

Frequency Dependence of the Electric Field Grading of End-Winding of Generator Bars

Torstein Grav Aakre, Henrik Enoksen, Espen Eberg, Athanasios Mermigkas and Jorunn Hølto

Abstract— To reduce the electric field stresses in the end-winding in hydropower generator bars, a field dependent grading tape is applied in the transition zone from outer corona protection to bare insulation. The design is typically optimized for 50/60 Hz with both low heat generation and optimal electric field distribution. The introduction of power electronic converters with high switching frequencies and dU/dt for controlling the generators changes the optimal design requirements. This work investigated experimentally the effect of higher voltage-frequencies on the conductivity in three field grading tapes from the same manufacturer with different field grading properties. The experimentally determined material parameters were then applied as inputs to finite element method (FEM) models to evaluate the electric field distribution at different voltage-frequencies. Measurements showed that the DC conductivity was highly nonlinear and strongly dependent on the electric field. This strong nonlinearity decreased at low electric fields as the frequency increased. The AC conductivity had a transition from a strong nonlinear material at line frequency to a less nonlinear material at 10 kHz. Simulations of the surface electric field and temperature using the DC conductivity for different voltage frequencies showed minor differences from simulations using the apparent AC conductivity. This indicates that the low field conductivity is of minor importance as it varied by two decades between DC and 10 kHz without resulting in a significant difference in either electric field, or temperature. The measured and simulated surface temperature increased linearly with applied voltage frequency. The simulated surface electric field was well distributed at line frequency, whereas it was greatly enhanced above 1 kHz.

Index Terms— Rotating machine insulation, variable frequency, field grading

I. INTRODUCTION

FIELD grading of generators is mandatory for machines rated greater than 6 kV [1], [2]. The resistive field grading is applied as e.g. wrapped tape or paint, and the conductive filler is mainly silicon carbide (SiC) [3]–[6]. The electric conductivity of SiC is nonlinearly dependent on the applied electric field [7], and therefore provides better field grading properties than alternative filler materials with constant or linear conductivity [8]. It is established practice to design the field grading with good properties to work at line frequency [2], [9].

As renewable energy sources are connected to the grid,

extensive use of power electronic converters (PEC) is expected in e.g. pumped hydropower generators for optimal pumping speed and load control. Today, the preferred topology is the voltage source converter (VSC) [10] with the use of semiconductor devices [11]. This means that pulse width modulation (PWM) is applied in variable speed hydropower plants [12]. These converters generate narrow rise time impulses with a high repetition rate [9], [13] which might reach the machine terminals [14]. To avoid premature failure caused by electric breakdown, the field grading design might need to be improved when generators and motors are connected to PECs. A high switching frequency with a steep voltage rise (dU/dt) results in considerably higher electric field levels and possible Joule heating [8], [9], [15], [16]. This implies that possible degradation and failure mechanisms are thermal hot spots [2], [17], surface corona discharge at local points with high electric field [15], [18], or degradation of the stress relief coating due to high temperature [4], [9].

The effect of high frequency square voltage waveforms on the field grading has been studied in e.g. [19]–[22], and the materials were found to neither control the electric field or resist heat production sufficiently at high frequency square voltage. The high nonlinearity in the field grading material makes it necessary to fully characterize the field and frequency dependent conductivity in order to perform modelling of the field grading system. A high conductivity gives a good field grading [2], but on the cost of a higher surface temperature and resulting degradation [20]. This issue thus becomes a trade-off between either low electric field or low heat production.

This paper experimentally investigates the frequency dependent apparent AC conductivity of three field grading tapes based on SiC, and their use in field grading at higher frequencies by using the original 50/60 Hz design. A finite element method (FEM) model is established to calculate the surface electric field and surface temperature. The calculations are verified by surface temperature measurements. This is done to investigate the high frequency dependence of the current field grading solution and find if there is a lower acceptable applied AC-frequency limit, as it is expected that the field grading is not effective at higher frequencies [23]–[25].

The authors are with SINTEF Energy Research, Department of Electric Power Technology, NO-7465 Trondheim, Norway

Color versions of one or more of the figures in this article are available online at <http://ieeexplore.ieee.org>

Digital Object Identifier: 10.1109/TDEI.2022.3214178

Manuscript received Month 05, 2022; accepted Month 10, 2022. This project has received funding from the European Union's Horizon 2020 "Secure, Clean and Efficient Energy" Programme, H2020-LCE-07-2016-2017, under grant agreement no 764011. Project: Increasing the value of hydropower through increased flexibility—HydroFlex. (Corresponding author: Torstein Grav Aakre e-mail: torstein.aakre@sintef.no)

II. MATHEMATICAL DESCRIPTION OF EXPERIMENTAL DATA

A. General Representation of a periodic Signal

Any periodic voltage waveform $v(t)$, with $v(0) = 0$, can be represented by its Fourier series

$$v(t) = \sum_{k=1}^{\infty} V_k \cdot \sin(k\omega t) \quad (1)$$

where V_k is the amplitude of the k^{th} harmonic, and ω is the angular frequency. Similarly, the corresponding current signal $i(t)$, with $i(0) \neq 0$, can be represented by its Fourier series

$$i(t) = \sum_{k=1}^{\infty} (a_k \cdot \cos(k\omega t) + b_k \cdot \sin(k\omega t)). \quad (2)$$

where the Fourier coefficients a_k and b_k represent a parallel capacitance C_p and resistance R_p , respectively, by

$$i(t) = i_C(t) + i_R(t) = C_p \frac{dv(t)}{dt} + \frac{v(t)}{R_p}. \quad (3)$$

It is thus possible to calculate the equivalent parallel series capacitance and resistance by comparing the sine and cosine Fourier components of the measured current by (3).

B. Material Conductivity

The current density j and the conductivity σ are proportional by the electric field E :

$$j = \sigma E. \quad (4)$$

The conductivity σ is dependent on properties at the microscopic level, which can be challenging to measure on the macroscopic level. It is therefore common to use an empirical DC conductivity model to describe more complex behavior compared to linear Ohmic materials. The following empirical relation was used in e.g. [22] for the nonlinear conductor.

$$\sigma_{DC} = A \cdot e^{BE^n} \quad (1)$$

where A , B , and n are experimentally determined numerical factors. For instance, the nonlinearity factor n was $2/3$ in [22] and 1 in [20]. A general temperature dependence is obtained by multiplying by the Arrhenius relation $\exp\left(-\frac{W_a}{k_B T}\right)$, where W_a is the activation energy, k_B is the Boltzmann constant and T the temperature in Kelvin.

At AC, there is an apparent AC conductivity σ_{AC} , which is comprised of the DC conductivity σ_{DC} and the imaginary part of the complex permittivity, $\varepsilon''\varepsilon_0$, representing the polarization loss, multiplied with the angular frequency ω :

$$\sigma_{AC} = \sigma_{DC} + \varepsilon''\varepsilon_0\omega. \quad (6)$$

The imaginary part of the complex permittivity ε'' is in general frequency dependent [26]. Several models exist to empirically describe the frequency dependence, e.g., Debye and Cole-Cole. According to [26]: 'It appears to be a general rule that the prevailing forms of frequency dependence are fractional power laws.', on both rising and falling edge of the loss peak. Then, by assuming a broad dielectric loss peak, (6) is for a limited frequency range simply modified to:

$$\sigma_{AC} = \sigma_{DC} + \varepsilon''\varepsilon_0\omega^m. \quad (7)$$

The general AC conductivity is thereby written as

$$\sigma_{AC} = A \cdot e^{BE^n - \frac{W_{a\sigma}}{k_B T}} + \varepsilon_0\omega^m \cdot C \cdot e^{-\frac{W_{a\varepsilon}}{k_B T}}, \quad (2)$$

where A , B , and C are constants, $W_{a\sigma}$ and $W_{a\varepsilon}$ are activation energies.

III. EXPERIMENTAL PROCEDURE AND MODELLING

The scope of the experimental procedure and modelling is to determine the effect of voltage-frequency on the electric field and heat losses. To accomplish this, the work is divided in three parts:

1. Measure relevant material properties as input to FEM modelling.
2. FEM modelling of the electric field distribution and temperature rise.
3. Measurement of the surface temperature to verify the FEM model.

A. Materials

Three different field grading tapes (FGTs) and one insulation tape from the same manufacturer have been chosen for this investigation and are listed in TABLE I. The naming 'Strong', 'Medium', and 'Weak' refers to the manufacturer's definition of conductivity strength in the FGT. Numerical values for the DC conductivity and complex permittivity of the insulation can be found in [27], whereas the frequency dependent apparent conductivity of the field grading tapes is measured in this work. The outer corona protection (OCP) layer was ensured to be highly conductive, in which it could be possible to approximate it as an equipotential surface at all tested frequencies. A too low conductivity of the OCP results in a voltage distribution along the OCP [20].

TABLE I

OVERVIEW OF USED MATERIALS

	Tape	Label
Field grading		Strong FGT
		Medium FGT
		Weak FGT
Semiconductive varnish		OCP
		Insulation

B. Test Objects

For thermal conductivity measurements flat disks of $3 \times 60 \times 60 \text{ mm}^3$ (FGT) or $6 \times 60 \times 60 \text{ mm}^3$ (mainwall insulation) were made. For permittivity measurements flat discs of $0.4 \times 100 \times 100 \text{ mm}^3$ (two layers) of the different materials were made. The samples were cured in accordance with the material manufacturer's instructions. It was assumed that the permittivity is isotropic, hence direction of layers was not taken into consideration.

The test objects for measuring the conductivity and surface temperature were created by first wrapping the insulation tape in a half-overlapping manner around the 10-mm brass cylinder, creating a helix structure with many layers, in total 3 mm thick. The insulation was then grinded to a smooth surface in order to have a profile comparable to simulations. The FGT was also wrapped around the insulation in the helix, half-overlapping,

structure. The final design of the test object is sketched in Fig. 1. The curing of the tapes was performed in accordance with the manufacturer's instructions. The FGT is anisotropic [19], but the complex geometry leads to uncertainties in measuring the anisotropic parameters along the helical tape structure. Two copper tapes were therefore wrapped around the test object to create the electrodes which was separated by 10 mm for measuring isotropic volumetric conductivity of the helical shape of the FGT. This is similar to the procedure used in [1]. The term 'volumetric' is omitted in the rest of the article.

The centre conductor is grounded. Hence, a higher capacitive current is expected compared to a specimen with ungrounded centre. The capacitive current is maximum when the resistive current is zero and this capacitive enhancement should thus not influence the resistive current significantly.

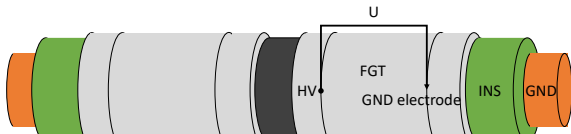


Fig. 1: Test object for measuring the FGT conductivity. The voltage is applied across U over 10 mm, and the central conductor is grounded.

C. Test Procedures

The thermal conductivity of the materials used was measured by the *Thermal Constants Analyser TPS 2500 S* (by HotDisk AB) using a sensor with radius 6.4 mm sandwiched between two flat disks of $3 \times 60 \times 60 \text{ mm}^3$ (FGT) or $6 \times 60 \times 60 \text{ mm}^3$ (mainwall insulation). The thermal conductivity was measured at 40°C , 60°C , and 90°C . The OCP layer is very thin, so it will have a minor impact on temperature distribution. The same value as mainwall insulation was therefore used.

The capacitance of plane FGT objects was measured at room temperature by an RLC-meter with an approximate electric field of 100 V/mm , measured at 1-10 kHz. The permittivity was calculated based on those results.

A sketch of the electrical circuit used to energise the test object is shown in Fig. 2. An AC voltage generated by a function generator and amplified by the *TREK 20/20C HS* high voltage amplifier is applied across the test object. This voltage is registered, while the current through the test object is amplified by the current amplifier *SR570* before being saved by a *GaGe CS8347* oscilloscope. A constant voltage amplitude of max $5.5 \text{ kV}_{\text{peak}}$ is applied at 10 kHz, limited by the 20-mA current of the amplifier. Next, the frequency was reduced in

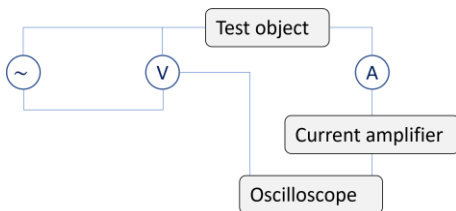


Fig. 2: Sketch of the electrification setup. An AC voltage is generated and applied across the test object. The voltage is measured directly, and the current through the test object is amplified before being measured by an oscilloscope.

steps down to 1 Hz. The voltage amplitudes and frequencies were chosen to be identical for both the experimental and the simulation work. The temperature was controlled by a heating cabinet.

The voltage amplitude was varied in initial tests. The calculated conductivity as a function of electric field within a single voltage period increased with increasing voltage amplitude. However, it was comparable at the highest voltage amplitudes tested, indicating that only parts of the tape were conductive at low voltages and assuming that the whole geometric volume conducted at the chosen voltage.

The setup for energizing the test object when measuring the surface temperature was identical to the measurement of conductivity, but with the voltage applied across the insulation. The surface temperature rise due to losses under voltage application was stable after 15 minutes and was then measured by 16 optical sensors using an optical thermal sensor system *Rugged Monitoring T301-08* connected to an *Agilent Data logger*.

D. FEM Model

The test object shown in Fig. 2 was used as a model system for numerical FEM simulations in COMSOL Multiphysics 5.6. The geometry was an axisymmetric 2D model, shown in Fig. 3, where the different materials are indicated by different colors. The key dimensions are listed in TABLE II and were chosen to fit the experimental test object. For the FGTs and insulation, the material properties used in the simulations were based on measured data included in this paper. Their thermal conductivities and electrical permittivities are listed in TABLE IV (average values used) and TABLE V, respectively. The electrical conductivity for the FGTs is modelled by (8) with parameter values listed in TABLE VI, whereas it is 10^{-14} S/m for the insulation [27]. The OCP is modelled with a high electrical conductivity of 1 S/m , relative permittivity 1, and thermal conductivity 0.46 W/(m K) .

TABLE II
DIMENSIONS USED IN FEM SIMULATIONS

	Dimension (mm)
Thickness of insulation	3.0
Thickness of OCP	0.4
Thickness of FGT	0.4
Distance from slot to FGT	20
Overlap between FGT and OCP	20

The electric field in the model calculated by

$$\nabla \cdot (\sigma + i\omega\epsilon_0\epsilon_r)\mathbf{E} = 0 \quad (9)$$

where the electric field caused by the electric potential V_a through $\mathbf{E} = -\nabla V_a$. Here, i denotes the imaginary unit. The temperature is calculated from

$$\rho C_p \frac{\partial T}{\partial t} = \nabla \cdot (k\nabla T) + Q_e \quad (10)$$

where ρ is the mass density, C_p is the specific heat capacity, k is the thermal conductivity, and $Q_e = \frac{1}{2} \text{Re}(\mathbf{J} \cdot \mathbf{E}^*)$ is the Joule heating.

The boundary conditions were as follows: A sinusoidal voltage of frequency f and amplitude V_a was applied to the copper conductor, and the steel was grounded. Frequencies from 50 Hz to 10 kHz were used with a maximum amplitude of 5.5 kV_{peak}. The thermal boundary condition was natural heat convection expressed as

$$q_0 = h(T_{\text{ext}} - T) \quad (11)$$

on the interface between the solid materials and air. Here, h is the heat transfer coefficient and T_{ext} is the ambient temperature. As there was no forced air circulation in the experimental part, the heat transfer coefficient was set to 20 W/(m²·K) [28], whereas the ambient temperature was 20 °C.

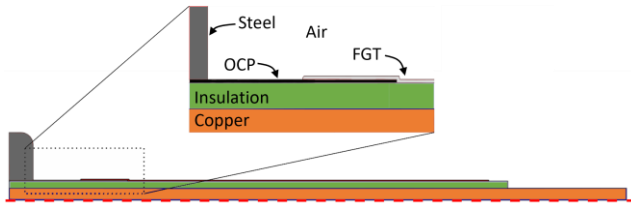


Fig. 3: Illustration of full geometry used in FEM simulations. Details of the overlap between the OCP and FGT are shown in the inset. The colors denote the different materials in this model. The red dashed line on the bottom is the axis of rotational symmetry.

The highest frequency of the electric field was 10 kHz meaning that the electrical time scale was less than 100 μs, while it took many minutes for any temperature change to be noticeable. It would require long computational times to simulate both electric and thermal physics at the same timescale since very short time steps were required for the electric field. Therefore, the simulations were performed in two steps. First, the stationary solution for the electric field was calculated. This was used as the input for the second step where a frequency-transient solver was used to find the stationary thermal solution. These two steps were solved for each combination of voltage frequency and amplitude. Splitting the simulation into two parts did remove the effect of the temperature increase on the electrical conductivity. However, the measured temperature dependence on the electrical conductivity was very small and could therefore be neglected in this analysis.

IV. RESULTS

A. Thermal Conductivity

Results from the measured thermal conductivity at different temperatures for the four investigated materials are shown in TABLE III. There is hardly any temperature dependence, thus the average values were used.

TABLE III

AVERAGE VALUE OF MEASURED THERMAL CONDUCTIVITY				
Temperature	Insulation	Weak FGT	Medium FGT	Strong FGT
°C	W/(m·K)	W/(m·K)	W/(m·K)	W/(m·K)
40	0.50	0.86	0.99	1.03
60	0.51	0.87	0.98	1.04
90	0.55	0.89	1.00	1.01
Average	0.52	0.87	0.99	1.03

For the main wall insulation, there is an agreement for the measured thermal conductivity with literature [20], whereas the FGT's thermal conductivity can vary greatly depending on both matrix material and filler particles used; [29] stating 0.6 – 5 W/(m K) for SiC composites, with new technologies raising conductivity even further [30].

B. Permittivity

The permittivities of the used materials were calculated based on measured capacitance with the RLC-meter. The results are summarized in TABLE IV.

TABLE IV
MEASURED RELATIVE PERMITTIVITY

	Permittivity
Strong FGT	5.9
Medium FGT	6.5
Weak FGT	7.2
Insulation	4.4

C. Measured Current

The measured current and voltage for one period is shown in Fig. 4 at 50 Hz, and in Fig. 5 at 10 kHz at 40 °C for the Strong FGT with voltage amplitude of 3.75 kV (i.e. 375 V/mm across

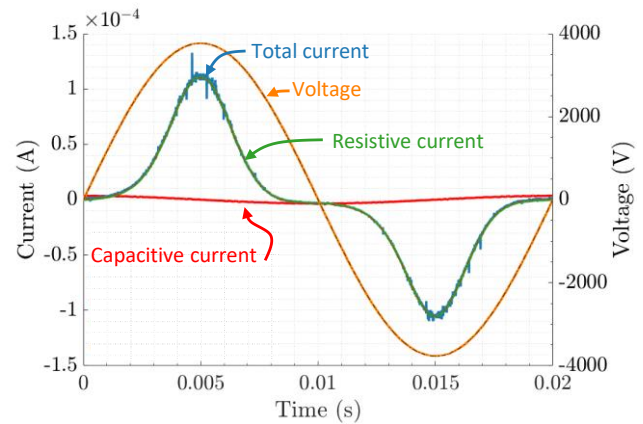


Fig. 4: Measured voltage and current for one period at 50 Hz and 40 °C for the Strong FGT. The electrodes are separated by 10 mm, thus the maximum electric field is 375 V/mm.

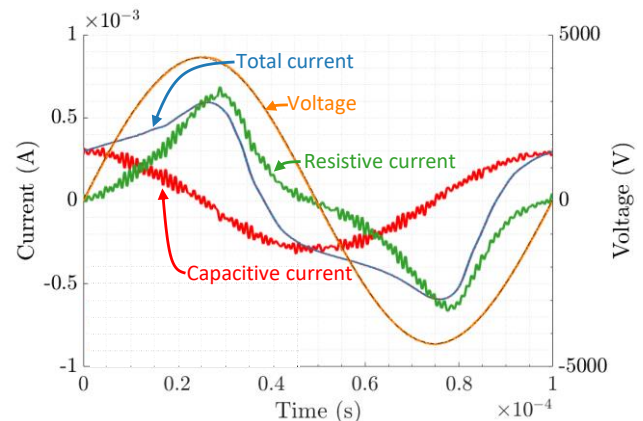


Fig. 5: Measured voltage and current for one period at 10 kHz and 40 °C for the Strong FGT. The electrodes are separated by 10 mm, thus the maximum electric field is 375 V/mm.

the measurement area). It can be seen that the current at 50 Hz is in phase with the applied voltage, thus totally dominated by the resistive current. On the other hand, the current at 10 kHz is highly influenced by the capacitive current in the object, including stray capacitances. The measured current must therefore be separated into one capacitive and one resistive part. This was done by using Fourier analysis to decompose the current in sine and cosine contributions (according to (2) and (3)). The voltage and current curves for the Medium FGT and Weak FGT are similar the curves in Fig. 4, and not shown here.

D. Calculated Volume Conductivity

The current density was found by dividing the measured resistive current by the measured voltage and distance (average electric field) by the FGT cross section ($2 \cdot 10^{-5} \text{ m}^2$). The calculated conductivity is therefore noisy at low electric fields. The high frequency noise was reduced by using the Fourier coefficients of the first 10 orders to remove high frequency noise and highlight the field dependence. The current density vs. electric field was then curve fitted to (4) and (8) for all frequencies and temperatures in a single routine for each of the three different FGTs to estimate the volume conductivity. The calculated values are shown in TABLE V. The temperature dependency is low, as an activation energy of $W_a = 7 \cdot 10^{-2} \text{ eV}$ yields a relative conductivity change of max 1.3 from 20 °C to 50 °C and can thus be omitted as this is low compared to other responses to frequency and electric field.

TABLE V

CURVE FITTED PARAMETERS FOR THE THREE FGTs TO (8).

	Strong FGT	Medium FGT	Weak FGT
A	$8.5 \cdot 10^{-8}$	$6.5 \cdot 10^{-8}$	$2.5 \cdot 10^{-8}$
B	$1.3 \cdot 10^{-5}$	$0.85 \cdot 10^{-5}$	$0.8 \cdot 10^{-5}$
n	1	1	1
$W_{a,\sigma}$	$7.47 \cdot 10^{-4}$	$7.18 \cdot 10^{-2}$	$7.67 \cdot 10^{-2}$
C	$9.0 \cdot 10^2$	$3.7 \cdot 10^2$	$3.0 \cdot 10^2$
m	3/4	3/4	3/4
$W_{a,\epsilon}$	$2.62 \cdot 10^{-2}$	$1.24 \cdot 10^{-2}$	$2.44 \cdot 10^{-2}$

The measured and modelled conductivity for the Strong FGT as a function of applied electric field is shown in Fig. 6. Higher fields could not be measured, and the observed trends have been extrapolated to higher fields strengths. The nonlinearity was most dominant at low frequencies and low fields, especially at 1 Hz. The nonlinearity at electric fields below 200 V/mm disappeared as the frequency increased. This can be modeled as a field independent complex permittivity, which is more prominent at higher frequencies due to the ω -dependence in (6). It is indicated from the exponent $m = 3/4$ in the frequency dependence that the relaxation mechanisms are complex and not straightforwardly described. The DC conductivity was totally dominating at high electric fields; thus, no frequency dependency was observed as there was no field dependence of the permittivity in the fitted equation. This resulted in an AC conductivity that had a transition from a strong nonlinear material at line frequency, to a linear material at 10 kHz which is worse in terms of field grading capabilities compared to 50/60 Hz [6]. The temperature dependence was weak and, thus, not expected to influence material properties compared to that of the frequency and electric field dependence.

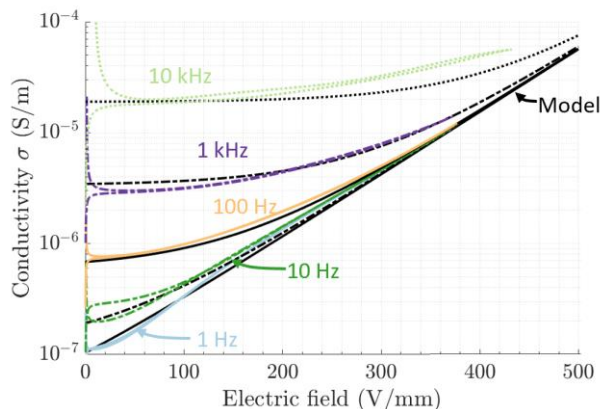


Fig. 6: Calculated conductivity at indicated frequencies as a function of electric field (colored lines), and curve fit to (8) in black lines. The Strong FGT is used as an example at 40 °C. High frequency noise was removed by only including harmonics up to 10th order of the signals.

V. MEASURED AND CALCULATED SURFACE TEMPERATURE AND ELECTRIC FIELD

A. Surface Temperature

The measured and simulated surface temperatures are given in Fig. 7 as a function of surface location at 50 Hz, 1 kHz, and 9 kHz (limited by the voltage source current constraints) for the Strong FGT. The overall trend was similar for the Medium and Weak FGT. The measured and simulated values followed the same trend, showing that the FEM calculations were reasonable. The spatial resolution of the temperature measurement was on the order of centimeter, which indicates that a potentially narrow temperature peak was not recorded and is a possible explanation for the large deviation between measured and simulated maximum temperature. Another possibility is that the conductivity is higher than the actual conductivity, which should lead to a higher temperature.

The maximum simulated surface temperatures as a function of voltage frequency are shown in Fig. 8 for the three FGTs. An interesting observation is the approximately linear increase in

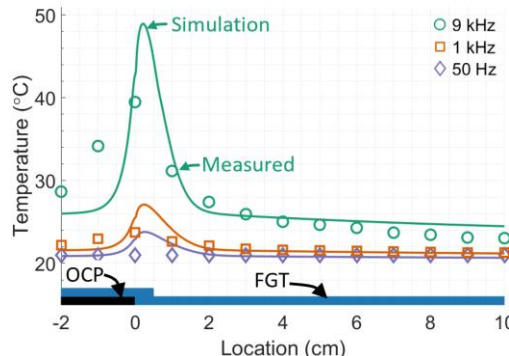


Fig. 7: Measured and calculated surface temperature at 5.5 kV_{peak} as a function of location at indicated frequencies for the Strong FGTs. Location '0' corresponds to the end of ground potential. Max 9 kHz was used due to voltage source current constraints.

temperature from 50 Hz to 10 kHz. The largest temperature increase was seen for the Strong FGT, as it had the highest conductivity. The applied voltage was below possible service voltage; hence the temperature rise would be even higher in operation and add to the temperature rise due to losses in the copper conductor. The Weak FGT has the lowest temperature increase as the conductivity was the lowest. Similarly, the Strong FGT had a high temperature increase at high frequencies and a high conductivity.

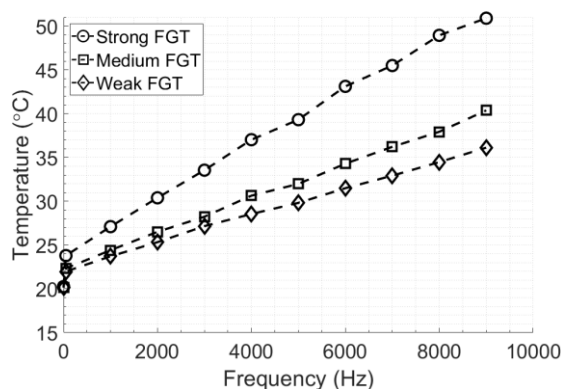
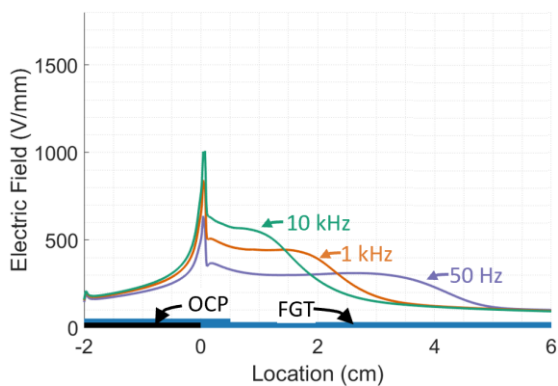
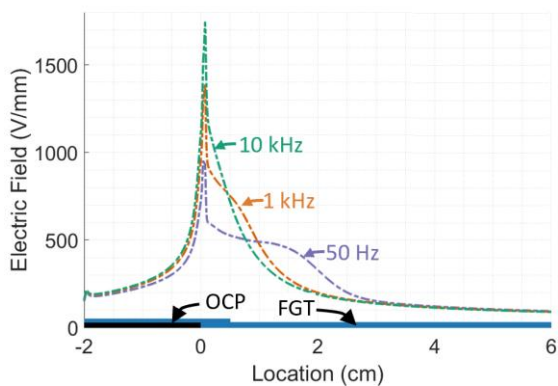


Fig. 8: Simulated maximum surface temperature as a function of frequency for the three FGTs at 5.5 kV_{peak}.



a) Strong FGT



b) Weak FGT

Fig. 9: Simulated surface electric field as a function of location for the Strong FGTs at 50 Hz, 1 kHz, and 10 kHz and 5.5 kV_{peak}.

B. Surface Electric Field

The surface electric field as a function of location at 5.5 kV_{peak} is shown in Fig. 9 for the Strong FGT with high conductivity and for the Weak FGT with low conductivity at 50 Hz, 1 kHz and 10 kHz. The Strong FGT reduced the maximum electric field more than the Weak FGT, as expected due to its higher conductivity. However, field grading capabilities were weakened as the frequency increased for both cases. It was observed that the field significantly increased even at 1 kHz. The electric field was elevated, though only at the first few centimetres close to the ground end.

The spatial dispersion of the electric field was here used as a measure on the goodness of the field grading of the FGT. It is shown as a function of frequency in Fig. 10. It can clearly be seen that there was a strong frequency dependence, as the field grading was basically weakened after the first hundreds of Hertz with little difference at frequencies above 5 kHz.

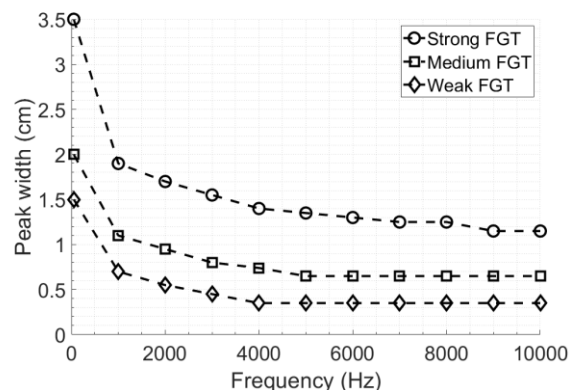
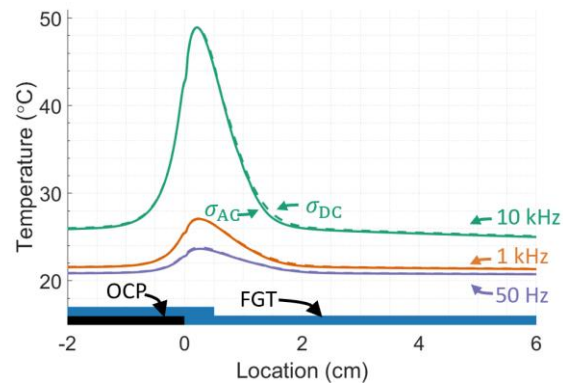


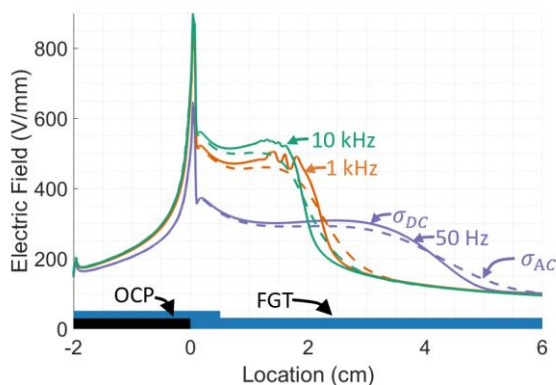
Fig. 10: Calculated plateau length (main peak width) of the surface electric field as a function of frequency (50 Hz to 10 kHz) for the three FGTs at 5.5 kV_{peak}.

C. Using AC or DC conductivity in Modelling

This paper used measurements of the apparent AC conductivity for FEM modelling as the conductivity is highly frequency dependent. However, measuring the apparent AC conductivity can be time consuming, and it would have been beneficial if it was sufficient to measure the DC conductivity only. Therefore, the difference of using the AC and DC conductivity was investigated by running the simulations for all frequencies with the curve fitted AC and DC conductivity in (8) for the cases when defining $\omega = 0$ rad/s (DC) and $\omega = 2\pi f$ rad/s (AC) in the equation. The resulting surface temperature and electric field at indicated frequencies for the Strong FGT using AC or DC conductivity are shown in Fig. 11. The results in these graphs showed that the surface temperature was hardly changed. The differences between using AC and DC conductivity were smaller than the differences between measured and simulated results. The electric field at 50 Hz was practically not influenced by the choice of conductivity, whereas the surface electric field at 1 kHz and 10 kHz were only slightly increased when using the DC conductivity instead of the AC one, suggesting that it would have been sufficient to use the DC conductivity in this case.



a) Surface temperature



b) Surface electric field

Fig. 11: Simulated surface temperature (a) and surface electric field (b) at indicated frequencies at 5.5 kV_{peak} for the Strong FGT. The curves are either based on the DC conductivity (solid lines) or the AC conductivity (dashed lines).

VI. DISCUSSION

The conductivity on three wrapped FGT systems have been measured, similar to what was done in [19]–[22]. A nonlinearity factor of $n = 1$ was found for all three FGT systems, in accordance with [20], whereas in [22] a lower value of $2/3$ was found. Such variation in results is expected as the nonlinearity factor is dependent on the manufacturer material choice, and which SiC grains were used [31]. The AC conductivity was earlier measured in [22] at selected frequencies up to 5 kHz. The overall trends were similar to what was measured here and shown in Fig. 6: A strongly field dependent DC conductivity and less field dependence at higher frequencies. The AC conductivity is significantly higher than the DC conductivity when the electric field is sufficiently low. The curve fit to (8) strongly indicates that the FGTs has polarization losses, which are not linearly dependent on frequency.

Reference [20] compared using the AC and DC conductivity in the model and concluded that the DC conductivity of the FGT cannot reflect the real performance of the field grading system under very high electric field when the field expanded beyond the FGT region. The results in Fig. 11 indicate that it is of minor importance whether DC or AC conductivity is used. The

resulting surface temperature and electric fields are comparable and difficult to differentiate when the FGT region is sufficiently long. It indicates that the low field conductivity is unimportant as it varied more than two decades without influencing the surface electric field or temperature. With the results from [20] in mind, it is important to think critically about the whole system if considering using the DC conductivity, only.

The field grading of generator bars is originally optimized for 50/60 Hz. The resistive field grading together with the capacitance from the insulation results in a frequency dependent response. That is, applying pulsed voltages with high frequencies alter the field grading response, thus resulting in higher electric field, and temperature. Works in literature have studied either 50 Hz or pulsed voltages with steep voltage rise and a high switching frequency [8], [19], [20]. The current work has additionally studied the direct influence of frequency up to 10 kHz on the characteristic properties of the FGTs. The maximum surface temperature increased linearly with frequency as shown in Fig. 8, whereas the plateau length of the surface electric field decreased logarithmically with frequency as shown in Fig. 10. This implies that the field grading is partly lost at frequencies as low as 1 kHz. This is for instance lower than the switching frequency of PWM [12].

VII. CONCLUSIONS

The volumetric conductivity was measured at selected electric fields, frequencies, and temperatures. The overall trend for the DC field dependence followed the main trend seen in literature; proportional to the exponential of the electric field $\exp(E)$ with minor temperature dependence. It has earlier been seen that the conductivity increases significantly when increasing the frequency. Now, the trend of this increase was found to be proportional to the frequency to the three-quarter power $\propto \omega^{3/4}$. Consequently, the apparent AC conductivity includes a part of polarization losses, which are not straightforwardly explained. These polarization losses are not field dependent; thus, a weaker field dependence was seen for the AC conductivity. Thus, the AC conductivity had a transition from a strong nonlinear material at line frequency to a less nonlinear material at 10 kHz. The transition occurred at lower fields for FGT with higher conductivity.

The surface temperature was both measured and simulated, based on measured conductivity. The results were comparable, but the peak value was different, probably due to coarse experimental spatial temperature sampling. The surface temperature increased almost linearly with voltage frequency, and at a higher rate when the FGT conductivity was high. This implies that there is no threshold frequency for temperature control, as the temperature is gradually increasing.

The conductivity is essential in modelling of the FGT. The apparent AC conductivity is equal the DC conductivity plus the frequency dependent losses. By using the DC conductivity only, thus omitting the frequency dependent losses, showed minor differences in calculated surface temperature and surface electric field compared to using AC conductivity. This implicates that the low field conductivity is of minor importance as the low field conductivity varied by two decades between DC and 10 kHz without resulting in a significant difference in either surface electric field or temperature at

IEEE TRANSACTIONS ON DIELECTRICS AND ELECTRICAL INSULATION

10 kHz. This might be the case when the FGT is sufficiently long, as literature has shown a significant difference when the FGT was too short.

The overall trends of the calculated surface electric field were in line with literature at line frequency, meaning good field grading. The frequency dependence was clearly seen as the electric field plateau became narrower and at a higher level when the frequency increased. The field grading became drastically weakened above 1 kHz, with less variation between 1 kHz and 10 kHz. This applied to all tested FGTs, meaning that the FGTs are working suboptimal at higher frequencies than 1 kHz.

REFERENCES

- [1] C. Staubach, T. Hildinger, and A. Staubach, "Comprehensive electrical and thermal analysis of the stress grading system of a large hydro generator," *IEEE Electr. Insul. Mag.*, vol. 34, no. 1, pp. 37–49, Jan. 2018, doi: 10.1109/MEI.2018.8246120.
- [2] Cigré and Comité d'études D1, *FIELD GRADING IN ELECTRICAL INSULATION SYSTEMS*. Paris: Conseil international des grands réseaux électriques, 2019.
- [3] L. Donzel, F. Greuter, and T. Christen, "Nonlinear resistive electric field grading Part 2: Materials and applications," *IEEE Electrical Insulation Magazine*, vol. 27, no. 2, pp. 18–29, Mar. 2011, doi: 10.1109/MEI.2011.5739419.
- [4] M. Pradhan, H. Greijer, G. Eriksson, and M. Unge, "Functional behaviors of electric field grading composite materials," *IEEE Transactions on Dielectrics and Electrical Insulation*, vol. 23, no. 2, pp. 768–778, Apr. 2016, doi: 10.1109/TDEI.2015.005288.
- [5] J. P. Rivenc and T. Lebey, "An overview of electrical properties for stress grading optimization," *IEEE Transactions on Dielectrics and Electrical Insulation*, vol. 6, no. 3, pp. 309–318, Jun. 1999, doi: 10.1109/94.775616.
- [6] T. Umemoto, Y. Otake, M. Yoshimura, T. Nada, and R. Miyatake, "Optimization of double-layer stress grading system for high voltage rotating electrical machines by electric field and thermal coupled analysis," *IEEE Trans. Dielect. Electr. Insul.*, vol. 27, no. 3, pp. 971–979, Jun. 2020, doi: 10.1109/TDEI.2019.008535.
- [7] A. Roberts, "Stress grading for high voltage motor and generator coils," *IEEE Electrical Insulation Magazine*, vol. 11, no. 4, pp. 26–31, Jul. 1995, doi: 10.1109/57.400761.
- [8] F. P. Espino-Cortes, E. A. Cherney, and S. Jayaram, "Effectiveness of Stress Grading Coatings on Form Wound Stator Coil Groundwall Insulation Under Fast Rise Time Pulse Voltages," *IEEE Trans. On Energy Conversion*, vol. 20, no. 4, pp. 844–851, Dec. 2005, doi: 10.1109/TEC.2005.853745.
- [9] F. P. Espino-Cortes, Cherney EA, and S. H. Jayaram, "Impact of inverter drives employing fast-switching devices on form-wound AC machine stator coil stress grading," *IEEE Electr. Insul. Mag.*, vol. 23, no. 1, pp. 16–28, Jan. 2007, doi: 10.1109/MEI.2007.288451.
- [10] M. Valavi and A. Nysveen, "Variable-Speed Operation of Hydropower Plants: A Look at the Past, Present, and Future," *IEEE Ind. Appl. Mag.*, vol. 24, no. 5, pp. 18–27, Sep. 2018, doi: 10.1109/MIAS.2017.2740467.
- [11] Y. Shakweh, "MV inverter stack topologies," *Power Engineering Journal*, vol. 15, no. 3, pp. 139–149, Jun. 2001, doi: 10.1049/pe:20010305.
- [12] M. Valavi, E. Devillers, J. L. Besnerais, A. Nysveen, and R. Nilsen, "Influence of Converter Topology and Carrier Frequency on Airgap Field Harmonics, Magnetic Forces, and Vibrations in Converter-Fed Hydropower Generator," *IEEE Trans. on Ind. Applicat.*, vol. 54, no. 3, pp. 2202–2214, May 2018, doi: 10.1109/TIA.2018.2801859.
- [13] J. C. G. Wheeler, "Effects of converter pulses on the electrical insulation in low and medium voltage motors," *IEEE Electrical Insulation Magazine*, vol. 21, no. 2, pp. 22–29, Mar. 2005, doi: 10.1109/MEI.2005.1412216.
- [14] Cigré and Comité d'études D1, *Insulation degradation under fast, repetitive voltage pulses*. Paris: Conseil international des grands réseaux électriques, 2017.
- [15] G. C. Stone and I. Culbert, "Review of stator insulation problems in medium voltage motors fed from voltage source PWM drives," in *Proceedings of 2014 International Symposium on Electrical Insulating Materials*, Niigata, Jun. 2014, pp. 50–53. doi: 10.1109/ISEIM.2014.6870717.
- [16] F. P. Espino-Cortes, S. Jayaram, and E. A. Cherney, "Stress grading materials for cable terminations under fast-rise time pulses," *IEEE Trans. Dielect. Electr. Insul.*, vol. 13, no. 2, pp. 430–435, Apr. 2006, doi: 10.1109/TDEI.2006.1624289.
- [17] F. P. Espino-Cortes, Y. Montasser, S. H. Jayaram, and E. A. Cherney, "Study of Stress Grading Systems Working Under Fast Rise Time Pulses," in *Conference Record of the 2006 IEEE International Symposium on Electrical Insulation*, Toronto, ON, Canada, 2006, pp. 380–383. doi: 10.1109/ELINSL.2006.1665337.
- [18] H. Hu, X. Zhang, Y. Liu, L. Guo, and J. Gao, "Optimization of the Electric Field Distribution at the End of the Stator in a Large Generator," *Energies*, vol. 11, no. 10, p. 2510, Sep. 2018, doi: 10.3390/en11102510.
- [19] E. Sharifi, S. Jayaram, and E. Cherney, "AC modeling and anisotropic dielectric properties of stress grading of form-wound motor coils," *IEEE Trans. Dielect. Electr. Insul.*, vol. 17, no. 3, pp. 694–700, Jun. 2010, doi: 10.1109/TDEI.2010.5492240.
- [20] A. Naeini, Edward. A. Cherney, and S. H. Jayaram, "Effect of conductivity on the thermal and electrical properties of the stress grading system of an inverter-fed rotating machine," *IEEE Trans. Dielect. Electr. Insul.*, vol. 26, no. 1, pp. 179–186, Feb. 2019, doi: 10.1109/TDEI.2018.007618.
- [21] A. Naeini, "A Study of Stress Grading System of Medium Voltage Motor Fed by Adjustable Speed Drives," p. 153, 2019.
- [22] E. Sharifi, S. Jayaram, and E. Cherney, "Temperature and electric field dependence of stress grading on form-wound motor coils," *IEEE Trans. Dielect. Electr. Insul.*, vol. 17, no. 1, pp. 264–270, Feb. 2010, doi: 10.1109/TDEI.2010.5412026.
- [23] T. Christen, L. Donzel, and F. Greuter, "Nonlinear resistive electric field grading part 1: Theory and simulation," *IEEE Electrical Insulation Magazine*, vol. 26, no. 6, pp. 47–59, Nov. 2010, doi: 10.1109/MEI.2010.5599979.
- [24] T. Bengtsson *et al.*, "Repetitive fast voltage stresses-causes and effects," *IEEE Electr. Insul. Mag.*, vol. 25, no. 4, pp. 26–39, Jul. 2009, doi: 10.1109/MEI.2009.5191414.
- [25] N. Taylor and H. Edin, "Stator end-winding currents in frequency-domain dielectric response measurements," *IEEE Trans. Dielect. Electr. Insul.*, vol. 17, no. 5, pp. 1489–1498, Oct. 2010, doi: 10.1109/TDEI.2010.5595550.
- [26] A. K. Jonscher, "Dielectric relaxation in solids," *J. Phys. D: Appl. Phys.*, vol. 32, no. 14, pp. R57–R70, Jul. 1999, doi: 10.1088/0022-3727/32/14/201.
- [27] T. G. Aakre, E. Ildstad, and S. Hvidsten, "Partial discharge inception voltage of voids enclosed in epoxy/mica versus voltage frequency and temperature," *IEEE Trans. Dielect. Electr. Insul.*, vol. 27, no. 1, pp. 214–221, Feb. 2020, doi: 10.1109/TDEI.2019.008394.
- [28] Y.A. Cengel, *Heat transfer: A practical approach*, 2nd ed. McGraw-Hill, New York.
- [29] W. Tong, *Mechanical Design of Electric Motors*. CRC Press, 2014. [Online]. Available: <https://books.google.no/books?id=DizNBQAAQBAJ>
- [30] M. C. Vu *et al.*, "High Thermal Conductivity Enhancement of Polymer Composites with Vertically Aligned Silicon Carbide Sheet Scaffolds," *ACS Appl. Mater. Interfaces*, vol. 12, no. 20, pp. 23388–23398, May 2020, doi: 10.1021/acami.0c02421.
- [31] L. Donzel, M. Montenegro-Uratsun, M. Hagemeister, and P. Rukwid, "ZnO stress grading tape for stator windings for electrical machines located at higher altitudes," in *Cigré Session 2016*, Paris, France, 2016, p. 12. [Online]. Available: https://e-cigre.org/publication/D1-107_2016